

# Single-protein nanomechanical mass spectrometry in real time

M. S. Hanay<sup>1‡</sup>, S. Kelber<sup>1‡</sup>, A. K. Naik<sup>1†</sup>, D. Chi<sup>1</sup>, S. Hentz<sup>1,2</sup>, E. C. Bullard<sup>1</sup>, E. Colinet<sup>1,2</sup>, L. Duraffourg<sup>2</sup> and M. L. Roukes<sup>1\*</sup>

**Nanoelectromechanical systems (NEMS) resonators can detect mass with exceptional sensitivity. Previously, mass spectra from several hundred adsorption events were assembled in NEMS-based mass spectrometry using statistical analysis. Here, we report the first realization of single-molecule NEMS-based mass spectrometry in real time. As each molecule in the sample adsorbs on the resonator, its mass and position of adsorption are determined by continuously tracking two driven vibrational modes of the device. We demonstrate the potential of multimode NEMS-based mass spectrometry by analysing IgM antibody complexes in real time. NEMS-based mass spectrometry is a unique and promising new form of mass spectrometry: it can resolve neutral species, provide a resolving power that increases markedly for very large masses, and allow the acquisition of spectra, molecule-by-molecule, in real time.**

Mass spectrometry—the identification of species by molecular mass measurements—is an important analytical tool in chemical and biological research. Since it was first applied to organic compounds more than half a century ago<sup>1,2</sup>, mass spectrometry has assumed an increasingly dominant role in life sciences and medicine, and is now arguably the mainstay of proteomics<sup>3</sup>. Mass spectrometers that are capable of high resolution in the mass range above several hundred kilodaltons have been used to elucidate the structure of complex protein assemblies<sup>4–7</sup>, but this mass range is at or beyond the limit of many conventional mass spectrometry techniques. The development of new, delicate sample-handling methods for molecular ionization/injection, enabling so-called ‘native’ mass spectrometry<sup>4,8</sup>, has been essential to permit large molecules or molecular assemblies to be transported, intact, from the fluid phase to the vacuum phase for subsequent analysis. Nanoelectromechanical systems (NEMS)-based mass spectrometry (NEMS-MS)<sup>9–17</sup> is sensitive to the inertial mass of neutral particles that accrete on the resonators, which makes it particularly well suited to studies that require minimal ionization to avoid structural changes in the protein under investigation<sup>4,8</sup>.

We have discussed the principles and ultimate practical limits of NEMS-based mass detection elsewhere<sup>18</sup>; here we briefly review the salient points. On adsorption onto a NEMS resonator, an individual analyte molecule or particle can precipitously downshift the resonant frequency of each vibrational mode (see Supplementary Information). This is the basis of the measurement. Theoretical limits to inertial mass resolution from frequency-shift detection can apparently be as small as the single-dalton level<sup>17</sup>; indeed, recent endeavors already report mass resolution at the few-hundred-dalton level<sup>15</sup>. However, central to our present work is that all measurements so far neither measure the mass of individual molecules or nanoparticles, nor can do so in real time. This is despite the impressive recent improvements in mass resolution and the detection of discrete adsorption events<sup>16</sup>. The reason for this is that the resonant frequency shift induced by analyte adsorption depends on both the mass of the analyte and its precise location of adsorption on the NEMS resonator.

The first NEMS-based mass spectrometer overcame this problem by delivering the analytes in a way that ensured they were adsorbed uniformly across the surface of a doubly-clamped NEMS resonator (for which the relation between adsorption position and frequency shift is well known)<sup>16</sup>. This allowed the constituents of simple mixtures to be determined after the collection of only several hundred single-molecule adsorption events. (For comparison, conventional mass spectrometry measurements typically involve the measurement of  $\sim 10^8$  molecules<sup>19</sup>.) The analysis involved fitting to the statistical ensemble of measured frequency shifts by a rather complex multidimensional minimization procedure to extract the weights of each constituent, that is, to deduce the mass spectrum<sup>16,20</sup>. These first results demonstrated the potential of NEMS-MS, but the complexity of this process precluded its application to arbitrarily complex mixtures. Moreover, it did not work in real time.

Here, we describe an approach that enables direct determination of the mass of each arriving molecule, in real time, as it adsorbs on the NEMS resonator<sup>21</sup>. Moreover, it is directly applicable to arbitrarily complex mixtures because it involves no assumptions about the sample mixture. This new approach is implemented by simultaneously tracking the resonant frequency of multiple modes of an individual NEMS resonator, then resolving the time-correlated, adsorption-induced frequency jumps in several of these modes. As mentioned above, the resonance frequency depends on both the mass of the particle and its adsorption position along the resonator. However, it is possible to determine the mass from the frequency shift by using information from multiple mechanical modes<sup>22–24</sup>.

Pairs of simultaneous jumps in the frequencies of two different modes herald a single-molecule adsorption event. Here, we present an analytical framework based on Euler–Bernoulli beam theory to deduce the nominal values of the mass and adsorption position of individual molecules/particles just after adsorption. Using the complete expression for mode shape enables the direct determination of the mass and position uncertainty of each arriving molecule or particle<sup>20,21</sup>. Our analysis provides a numerical as well as a universal graphical approach to calculate the mass and

<sup>1</sup>Kavli Nanoscience Institute and Departments of Physics, Applied Physics, and Bioengineering, California Institute of Technology, MC 149-33, Pasadena, California 91125 USA, <sup>2</sup>CEA, LETI, MINATEC Campus, 17 rue des Martyrs, 38054 Grenoble Cedex 9, France; <sup>†</sup>Present address: Centre for Nano Science and Engineering, Indian Institute of Science, Bangalore, Karnataka, India; <sup>‡</sup>These authors contributed equally to this work. \*e-mail: roukes@caltech.edu

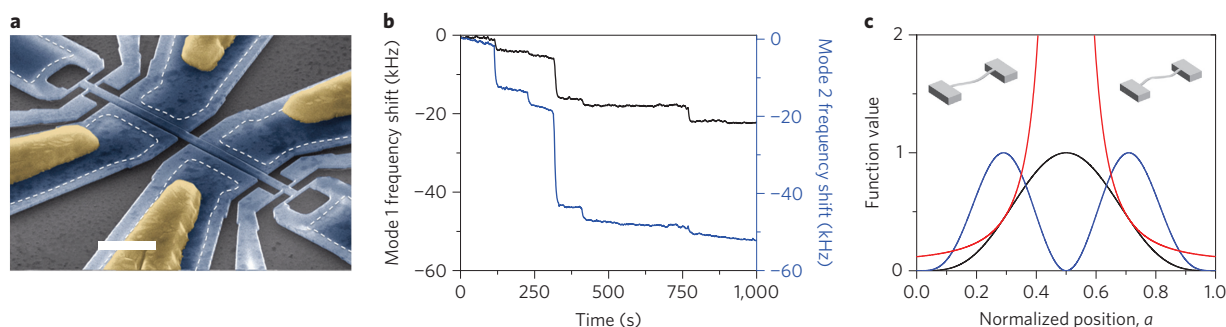


**Figure 1 | Multimode NEMS-based mass detection in real time.** **a**, Colourized electron micrograph of a representative device used in this study. The white dotted line shows the boundaries of the region beneath the suspended device that anchors it to the substrate. Yellow regions represent Al/Si gate contacts. Narrow gauges near the ends of the beam become strained with the motion of the beam, thereby transducing mechanical motion into electric resistance. Scale bar, 2  $\mu\text{m}$ . **b**, Plots of frequency shift versus time for the fundamental mode of our doubly-clamped resonator (mode 1: black line, left axis) and the second mode (mode 2: blue line, right axis) clearly showing the simultaneous shifts in frequency as individual gold nanoparticles land on the resonator. These modes have initial frequencies of 44.6 MHz and 105.0 MHz, respectively. **c**, Responsivity of mode 1 (black) and mode 2 (blue) as a function of position along a doubly-clamped resonator, and their ratio  $G$  (red line). Insets: schematics showing the mode shapes 1 (left) and 2 (right).

position of the analyte molecule, which arrives randomly in time and position.

### Multimode theory for single-molecule mass measurements

A point analyte of mass  $\delta m$ , such as a single molecule or particle, downshifts the resonant frequency of a nanomechanical resonator with mass  $M$  according to

$$\frac{\delta f_n}{f_n} = -\frac{\delta m \phi_n(a)^2}{M \alpha_n} \quad (1)$$

where  $f_n$  is the resonant frequency of the  $n$ th mode and  $\delta f_n$  is the frequency shift for this mode. Their ratio ( $\delta f_n/f_n$ ), the fractional frequency shift, is proportional to the fractional mass change  $\delta m/M$ .  $\phi_n$  denotes the mode shape for the  $n$ th mode, and  $a$  denotes the position of adsorption of the molecule on the beam (normalized to unitary beam length). The numerical constant  $\alpha_n$  depends on the mode number  $n$  and is of order unity. (See Supplementary Information for a more complete description.)

For a symmetric NEMS doubly-clamped beam, resolving the adsorbate-induced frequency shifts in the first two modes is adequate to determine the mass of the analyte molecule and its position of adsorption (Fig. 1; see Supplementary Section S1). The ratio of the responsivities of two arbitrary modes,  $G(a) \equiv \phi_n(a)^2/\phi_m(a)^2$ , determines whether their simultaneous measurement is sufficient for real-time mass detection. If  $G$  is invertible, then a unique value for the position, and therefore the mass of the molecule, can be obtained. Although this condition is not fulfilled for the first two modes of a doubly-clamped beam (Fig. 1c), analysis can be restricted to one half of the beam length due to the inherent symmetry of such a structure, and this permits the determination of a unique molecular mass and adsorption position relative to the beam centre (Supplementary Section S1).

In this Article, we use the first two modes of the NEMS device for mass measurements of individual protein macromolecules (IgM antibody isoforms) and individual gold nanoparticles. Each species that physisorbs onto the cooled NEMS device produces a distinct frequency shift in each mode of interest (Fig. 1b). As described in the following, these time-correlated frequency shifts are then used to determine both the mass and position of adsorption for each of the newly arrived analyte molecules or particles, as well as their corresponding uncertainties.

Given the aforementioned symmetry of the mode shapes, we restrict our analysis to one half of the beam,  $0 < a < 0.5$ . For this branch, the transformation  $G$  from the fractional-frequency shift pair ( $\delta f_1/f_1$ ,  $\delta f_2/f_2$ ) to the analyte mass-position pair ( $\delta m/M$ ,  $a$ ) is

one-to-one. Figure 2 graphically represents the transformation of experimentally observed, time-correlated frequency jumps from the first two modes of a doubly-clamped beam into mass and position of adsorption for each arriving analyte. The real-time experimental data, that is, frequency jumps for the two modes, are represented as fractional-frequency pairs ( $\delta f_1/f_1$ ,  $\delta f_2/f_2$ ). In this representation, the transformation yields analyte position contours that appear as straight lines passing through the origin, and the deduced mass contours appear as quasi-elliptical curves.

In a noiseless measurement, each analyte landing on the NEMS would be identified as a perfectly sharp single point in the  $|\delta f_1/f_1|, |\delta f_2/f_2|$  plane. However, in practical experiments, the mass and position of the analyte can only be determined up to certain confidence level that is determined by the frequency instabilities of the two separate, phase-locked modes of the NEMS resonator. These frequency fluctuations are characterized by their respective Allan deviations<sup>25</sup>.

To represent the frequency instability in a single-mode measurement, the induced frequency shift in each mode is modelled as a random variable with mean value commensurate with the measured jump and dispersion identical to that of the frequency noise. For multimode measurements, the frequency noise statistics for the separate modes are combined into a joint probability density function (JPDF) representation,  $\text{JPDF}_{\delta f_1/f_1, \delta f_2/f_2}(\delta f_1/f_1, \delta f_2/f_2)$ . Using a bivariate PDF transformation<sup>26</sup>, the  $|\delta f_1/f_1|, |\delta f_2/f_2|$  plane is mapped onto the  $(\delta m/M, a)$  plane and a JPDF for mass and position,  $\text{JPDF}_{\delta m, a}(\delta m, a)$ , is calculated (see Supplementary Information).

The JPDF of each analyte in the multimode space describes an elliptically shaped distribution, with the length of the principal axes corresponding to mass and position uncertainties. This two-dimensional JPDF can be projected onto either the mass or the position axis to determine the probability distribution of mass or position, respectively:

$$\text{PDF}_{\delta m}(\delta m) = \int_{a=0}^{a=0.5} \text{JPDF}_{\delta m, a}(\delta m, a) da \quad (2)$$

$$\text{PDF}_a(a) = \int_{\delta m=0}^{\delta m=\infty} \text{JPDF}_{\delta m, a}(\delta m, a) d(\delta m) \quad (3)$$

These noise-transformation relations can be used to systematically analyse the performance of NEMS-MS experiments. For example, mass resolution as a function of analyte position of adsorption can be obtained (Supplementary Figs S3 and S4).

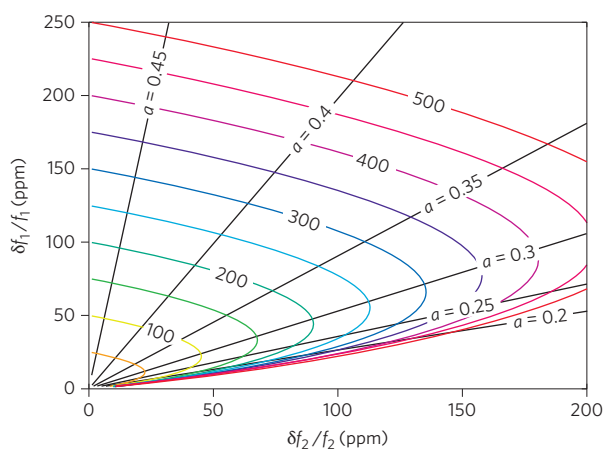


**Figure 2 | Determining analyte mass and position of adsorption from time-correlated, two-mode frequency jump data.**

Universal mass and position contours. The y- and x-axes represent the fractional frequency jumps,  $|\delta f_1/f_1|$  and  $|\delta f_2/f_2|$ , measured for modes 1 and 2, scaled in parts per million (ppm). The parametric curves represent the following. Straight black lines denote constant values of adsorption position, where  $a$  is the normalized position on the resonator and  $a = 0$  and  $0.5$  (both not shown) represent one end of the resonator and the centre of the resonator, respectively. The elliptical curves represent contours for constant adsorbate mass and are labelled in units of  $m_p/M$  and scaled in ppm. These parametric curves are valid for the first two same-plane modes of a doubly-clamped beam, and assume only Euler-Bernoulli beam theory.

### Experimental technique for NEMS-MS

The analysis outlined above was used to perform mass spectrometry on individual IgM antibody isoforms and gold nanoparticles using two separate and complementary experimental systems. These systems make use of distinct analyte injection/ionization schemes—electrospray ionization (ESI) and matrix-assisted laser desorption ionization (MALDI)—the results of which agree with one another (Fig. 4a). The NEMS resonators used in the experiments were optimized for the actuation and detection of the first two modes of a doubly-clamped beam<sup>27,28</sup>. (Further details are given in the Supplementary Information.)

The device (Fig. 1a) was fabricated using complementary metal-oxide-semiconductor (CMOS)-compatible, top-down processes designed for very-large-scale integration of NEMS<sup>29</sup>. Electrostatic actuation was achieved using proximal capacitive gates, and resonator motion was transduced using symmetric semiconducting piezoresistive strain gauges located near both ends of the device. Actuation and detection channels of the two modes were combined using high-frequency electronic components, and a feedback loop<sup>30</sup> was implemented using the General Purpose Interface Bus (GPIB) protocol. (See Supplementary Information for a schematic of the measurement and actuation circuit, as well as a summary of the device characteristics.)

The Allan deviations characterizing the frequency fluctuations of the first and second NEMS modes were  $\sigma_A^{(1)} \approx 8 \times 10^{-8}$  and  $\sigma_A^{(2)} \approx 1 \times 10^{-7}$ , respectively, at the chosen phase-locked loop (PLL) response time of  $\tau_R \approx 500$  ms, unless noted otherwise. For measurements of the 10 nm gold nanoparticles using the ESI system, obtained with a previous generation of smaller devices, these values were  $\sigma_A^{(1)} \approx 3 \times 10^{-6}$  and  $\sigma_A^{(2)} \approx 2 \times 10^{-6}$  at  $\tau_R \approx 10$  s. (A longer response time was required with the earlier generation of instrumentation used.) These frequency fluctuations yield a mass resolution of  $\sim 50$  and  $100$  kDa for these two sets of measurements, respectively. With our current third-generation instrumentation, not yet deployed for mass spectrometry, we have demonstrated a submillisecond time resolution.

The measured noise correlation between the modes was  $\sim 0.3$  ( $\sim 0.7$  for the first-generation system and devices). Figure 1b presents a snapshot of two-mode PLL data obtained during ESI of 10 nm gold nanoparticles (two-mode PLL data from the IgM run is shown in Supplementary Fig. S11). Time-correlated, quasi-instantaneous frequency jumps of different heights in the two modes clearly demonstrate our ability to resolve discrete adsorption events from individual molecules or nanoparticles accreting onto the NEMS resonator. These experimentally obtained frequency jumps were subsequently used to determine the mass and position of each molecule/nanoparticle by mapping the  $(\delta f_1/f_1, \delta f_2/f_2)$  pairs onto the  $\delta m/M, a$  plane, as previously described.

Figure 3a shows the mass and position of each adsorbing particle, as well as their respective uncertainties, for an experiment where 5 nm gold nanoparticles were delivered onto the NEMS mass sensor by means of MALDI. The mass spectrum was obtained by integrating the data along the position coordinate. The gold nanoparticles, as is usual in typical experimental samples, are known to have a large variance in radius, which translates into the very large mass spread observed ( $m \approx r^3$ ). If the gold nanoparticles were relatively monodisperse, the data would be expected to appear as relatively narrow bands along the mass axis. This kind of behaviour is well modelled by our Monte Carlo simulations of 5 nm and 10 nm gold nanoparticles if we assume low size variance and no clustering (Fig. 3b). Note that particles (or molecules) with smaller masses will produce smaller relative frequency shifts and, in the presence of a fixed amount of frequency noise, this will appear as a larger position uncertainty.

A counterintuitive feature of these spectra is the evident decrease in position uncertainty for heavier species, although the mass uncertainty remains constant. This originates from the fact that the mass resolution depends on the minimum resolvable frequency shifts, which again remain constant due to the frequency noise, regardless of the magnitude of the actual shifts from the arriving analytes. However, position resolution depends on the minimum resolvable angle in the  $(\delta f_1/f_1, \delta f_2/f_2)$  plane, and this improves as the magnitude of the frequency shifts becomes larger (Supplementary Fig. S9). The number of events observed near the centre of the beam is reduced because the second mode has a node at the centre, so particles landing in this region produce jumps below the noise level.

### Gold nanoparticle measurements

The mass spectra of 10 nm gold nanoparticles are shown in Fig. 4a for the data acquired from the ESI (black curve) and MALDI (blue curve) set-ups. To more easily make a comparison with the ESI data, the data for the MALDI curve shown here were analysed with the same experimental mass resolution as achieved with the ESI set-up for 10 nm gold nanoparticles. Also shown are the best-fit curves for each data set. For the ESI data, the best fit yielded a diameter of 9.8 nm and a standard deviation of 2.5 nm, while the data using MALDI yielded a diameter of 10.7 nm and a standard deviation of 2.8 nm. These values are within the experimental deviation of the vendor specifications for the gold nanoparticles. (See Supplementary Information for details of our fitting protocols.)

We complemented these 10 nm gold nanoparticle measurements with MALDI-based measurements on 5 nm gold nanoparticles. For these latter experiments, two types of MALDI plates were prepared, each containing 5 nm gold nanoparticles, but differing in whether glycerol was added as a separating agent (see Methods). Previous studies have demonstrated that the clustering effects typically exhibited by metallic nanoparticles can be mitigated by the addition of various separating agents<sup>31–34</sup>. Figure 4b presents two distinct mass spectra for the two 5 nm gold nanoparticle samples, which show a clear reduction in gold nanoparticle clustering when glycerol is used. To gain further insight into the observed cluster peaks, we

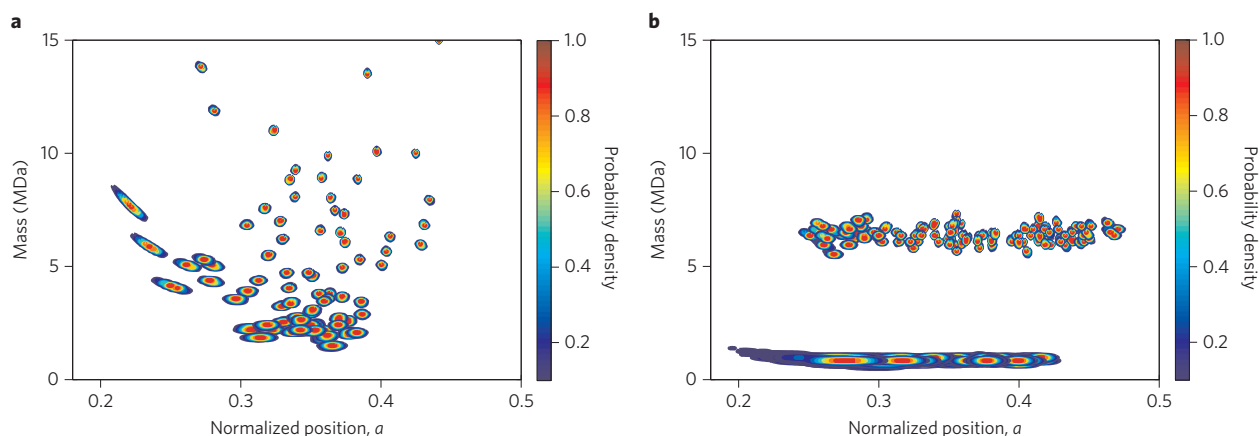


**Figure 3 | Joint probability distributions for analyte mass and adsorption position.** **a**, Experimental data for 5 nm gold nanoparticles from the MALDI experiment. Each analyte captured by the NEMS resonator has an error disk that reveals the uncertainty in its mass and adsorption position on the resonator. **b**, Monte Carlo simulations of 5 and 10 nm gold nanoparticles assuming a much lower size variance ( $\sim 2\%$ , no clustering) than the actual samples ( $\sim 15\text{--}20\%$ , with clustering). These simulations reveal the mass ‘bands’ that would be expected for nearly monodisperse gold nanoparticle distributions.

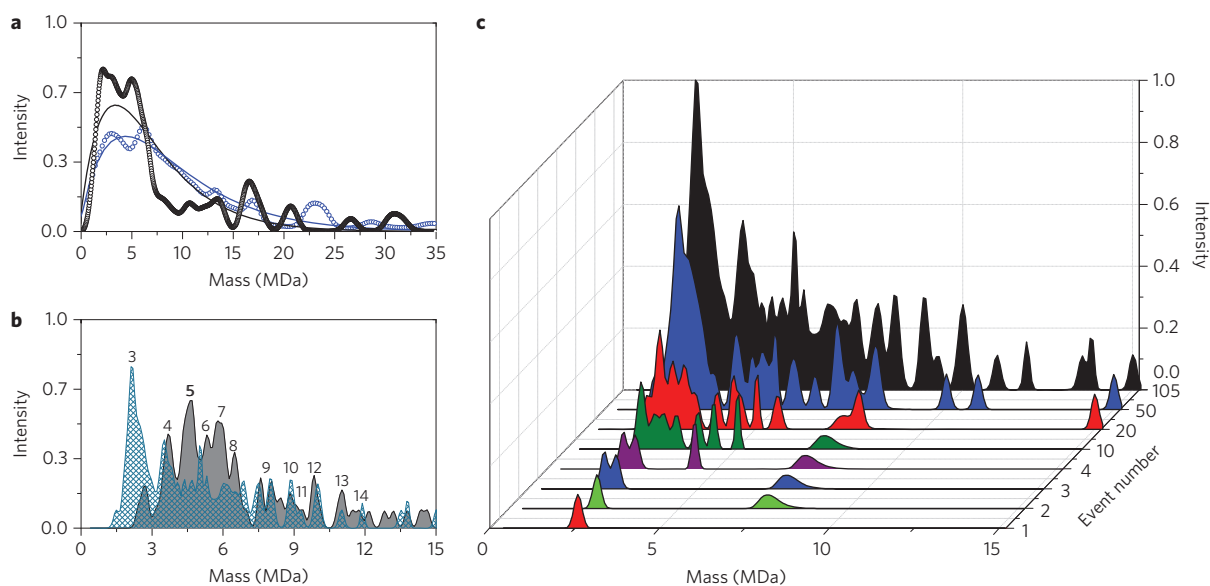


**Figure 4 | Mass spectra for 5 nm and 10 nm gold nanoparticles.** **a**, Mass spectra of 10 nm gold nanoparticles from the ESI set-up (open blue circles) and from the MALDI set-up (open black circles). Solid lines represent best fits to the data. The best fit for the ESI data is  $d = 9.8$  nm,  $\sigma = 2.5$  nm, and the best fit for the MALDI data is  $d = 10.7$  nm,  $\sigma = 2.8$  nm. **b**, Mass spectra of 5 nm gold nanoparticles from the MALDI set-up showing results for samples prepared without glycerol (grey) and with 10% glycerol (blue); the declustering effect from glycerol addition is evident. Peaks are labelled according to cluster size (for example, the mass of three, four and five particles, and so on). **c**, Mass spectra of the ensemble of 5 nm gold nanoparticles with glycerol as they arrive sequentially on the NEMS sensor. Each particle is represented as a spread in mass due to the measurement uncertainty. The event number refers to the number of particles that have accreted on the device up to that point. The total, cumulative spectrum (black) is the additive result for 105 individually measured particles.

modelled the clustering phenomena using Monte Carlo simulations (the details underlying our analyses are described in the Supplementary Information). Figure 4c shows the accumulated mass spectra, acquired particle by particle, for the 5 nm gold nanoparticles.

Each event in the current set of measurements provides the mass of the adsorbed analyte. This contrasts with previous measurements<sup>15,16</sup> where each data point was, at best, part of a statistical ensemble, itself one bit of information convolved with the position dependence of the single-mode NEMS response. Here, as is graphically displayed in Figs 4c and 5a, spectra can now be built up, particle by particle, as each analyte arrives. With this advance it is now possible to weigh individual molecules in real time, without the need

to first collect an ensemble of identical particles. This enables a straightforward analysis of complex mixtures, as exemplified in Fig. 5, and is the first time isolated biomolecules have been weighed by a nanomechanical device.

#### Human IgM antibody measurements

To further demonstrate the utility of NEMS-based mass spectrometry for biological species, we obtained single-molecule NEMS-MS spectra for human IgM using ESI injection. In serum, IgM is typically found in macromolecular complexes that are assembled by the immune system. The presently known biologically active isoforms in serum can be tetrameric, pentameric, hexameric or dipentameric assemblies of identical  $\sim 190$  kDa subunits<sup>35–38</sup>. For

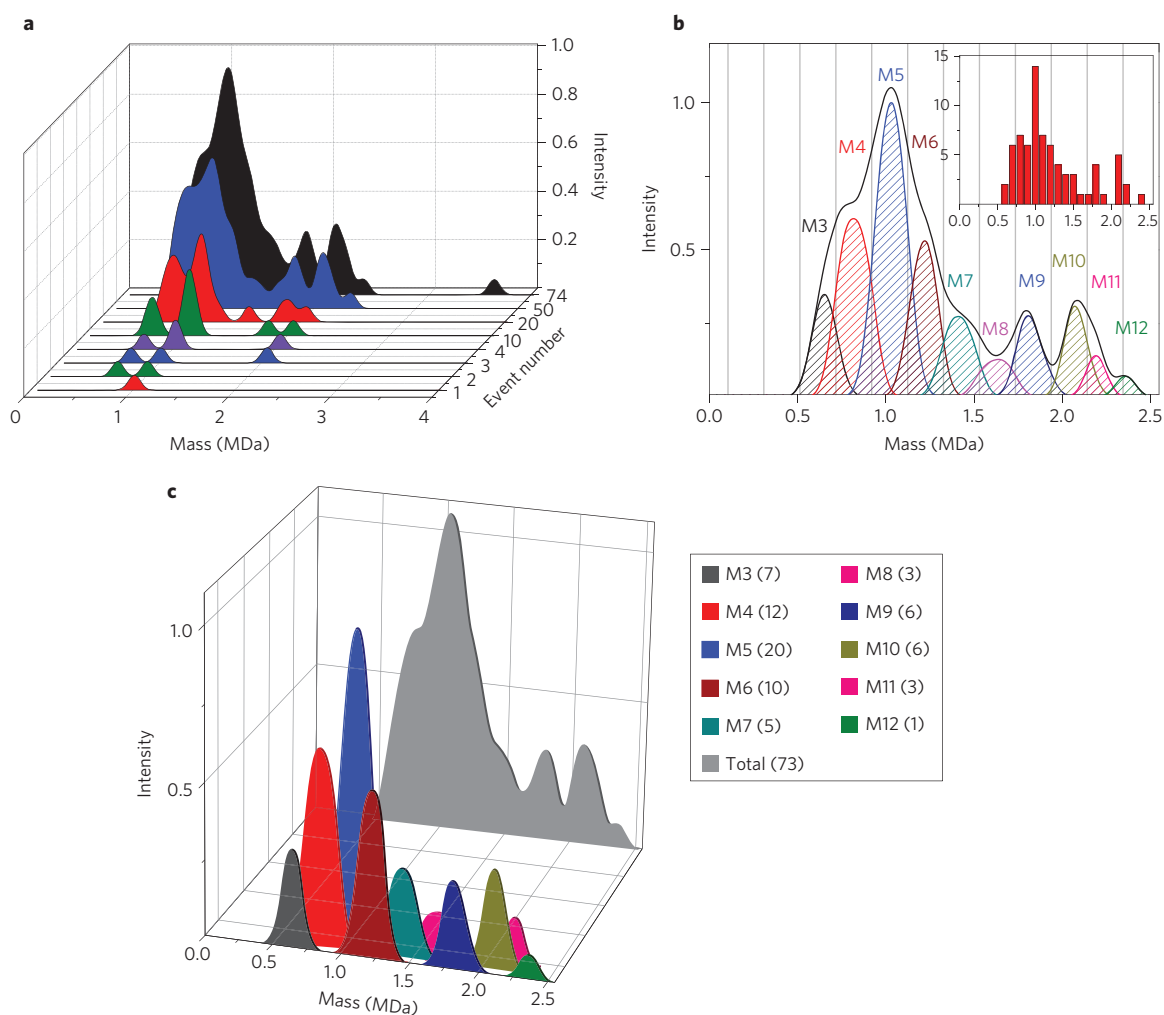


**Figure 5 | Nanomechanical mass spectra for human IgM.** **a**, Molecule-by-molecule acquisition of the mass spectra for human IgM. Analytes accumulating at different molecular weights correspond to different isoforms of the molecule. The final spectrum shown in black is the additive result of individual mass measurements for 74 accreted molecules and has readily identifiable sharp peaks that correspond to the major isoforms of IgM typically found in human serum. **b**, Decomposition of the IgM spectra into different polymerization levels. Grey lines delineate the cutoff thresholds used in assigning the different forms of IgM. The most dominant form of IgM in human serum is the pentameric form (M5), which has a molecular weight of  $\sim 1$  MDa and is observed as the global maximum of the NEMS-MS spectra. Subpopulations of other forms are also observed at masses corresponding to M3, M4 and M6–M12. Inset: histogram of the event masses binned according to mass resolution. The vertical axis of the inset corresponds to the number of events, and the horizontal axis is the mass in MDa. **c**, Mass spectra of individual subunits displayed quantitatively with single-molecule accuracy. Intensity peaks of different polymerized forms of IgM (M3–M12) yield the mathematically integrated composite mass spectrum (light grey) of the IgM sample. The numbers in parentheses to the right show the number of measured molecules for each isoform.

the prevalent pentamer isoform, an additional small protein (the J chain) helps link the assemblage and contributes  $\sim 15$  kDa to the total  $\sim 960$  kDa mass of the complex<sup>39,40</sup>. Our overall mass spectrum, a composite curve accumulated from 74 single-particle spectra, is shown in Fig. 5a. The individual pentameric IgM complex (the highest intensity peak) is clearly visible at  $1.03 \pm 0.05$  MDa, as is a dimerized pentameric complex (‘dipentamer’) at  $2.09 \pm 0.05$  MDa (their mass ratio very close to 2, as expected). These measured values are very close to the anticipated values 0.96 MDa and 1.92 MDa (ref. 40), which is remarkable given that we report mass values without any calibration other than using the nominal mask dimensions of our mass sensor (see Supplementary Information).

The apparent smoothness of the mass spectra for the individual isoforms of Fig. 5 arises from the fact that each single-particle/molecule event can be resolved with its own uncertainty level. Specifically, the mass spectra in Figs 4 and 5a represent information acquired from sets of 105 and 74 single-particle/molecule

adsorption events, respectively. Each of these events can be represented in the mass–position plane as a continuous probability distribution. Subsequently, we obtained mass spectra for each event by projecting the individual distributions onto the mass plane. For each particle/molecule accreted, this yields a smooth Gaussian-like curve for its mass spectrum, with a width dependent on the device frequency noise and position of the particle. The cumulative mass spectra are then Gaussian-like mass distributions averaged by like IgM isoforms, as in the foreground of Fig. 5c, or added overall to generate a composite spectrum, as in the background grey curve of Fig. 5c. Alternatively, one can report the centre of the mass distribution (as done in the inset of Fig. 5b), but one then loses the unique position and mass uncertainty information for each particle, as obtained with our uncertainty analysis formalism.

Figure 5b,c illustrates the power of single-molecule NEMS-MS to resolve spectra. Because the mass of each molecule is individually measured (and using prior knowledge of the IgM isoformal structure), each molecule can be identified based on its mass as an

IgM isoform. In a surprising reversal of the traditional situation, it is now possible to examine the underlying structure of the composite intensity curve. For instance, the apparent shoulder at 0.82 MDa in the composite intensity curve is seen to arise from the presence of precisely 12 accreted macromolecular complexes. Each is a tetramer of IgM that individually registers on the NEMS mass sensor and was separately measured as part of the ensemble of 74 molecules collected during this experiment. The legend to the right in Fig. 5c provides the number of molecules collected for each of the subunit peaks. To identify the different IgM isoforms with our single-molecule measurements, equidistant thresholds were used between the expected mass values of adjacent species, shown as grey lines in Fig. 5b. Because of our mass measurement error, there is a small probability for some events to be misidentified when the noise level during that particular event happens to exceed the  $2\sigma$  noise threshold separating two distinct species. We determined the number of potentially misidentified particles by performing a statistical analysis on the data ensemble (see Supplementary Information). This analysis suggests that less than 7% of events, that is, only  $\sim 5$  of the 74 collected molecules, might be misidentified.

Our experiment reveals a sequence of IgM isoforms from trimer ( $N=3$ ) up to dodecamer ( $N=12$ ) within the mass range investigated (excluding the solitary event at 3.6 MDa); these can originate from both physiological and experimental factors. Fragmentation and non-specific reassembly of large macromolecular species is expected to occur in ESI systems<sup>5,41</sup>. However, it is known that IgM can also be selectively assembled by the lymphatic system into pentamer and hexamer complexes as part of an immunologically driven response to antigens<sup>35,36</sup>. NEMS-MS, unlike conventional mass spectrometry, does not require the charging of analytes to achieve its selectivity. The ability to use neutral injection methods that capitalize on the strengths of NEMS-MS will, in the future, allow the direct determination of the efficiency of such immunological processes and allow them to be monitored in real time and, for example, in response to potential therapies, without the confounding source of isoforms arising from charge-driven fragmentation.

## Conclusions

We have demonstrated the potential of NEMS-based mass spectrometry by measuring the mass of individual protein macromolecules in real time. In particular, NEMS-MS systems can access masses above 500 kDa, whereas the performance of conventional mass spectrometry systems degrades at high masses. Improving the mass resolution of top-down fabricated nanomechanical devices by only one or two decades—which is attainable in the near term—offers exciting prospects for useful applications in bacterial identification, native mass spectrometry and structural identification of large macromolecules. Recent work has significantly improved the mass resolution of bottom-up fabricated NEMS devices<sup>13–15</sup> and now offers realistic potential for ultimately creating NEMS-MS spectrometers with resolution down to a few daltons. However, much work remains: bottom-up NEMS devices and approaches have yet to demonstrate mass measurements of individual molecules, and questions remain about their compatibility with large-scale integration. Ultimately, however, the capability of using very-large-scale-integration- (VLSI-) and CMOS-compatible NEMS with devices providing single-dalton sensitivity will enable the measurement of millions of proteins—in real time—from a small discrete sample (like a single cell) while retaining single-protein precision over the full range of biological interest.

## Methods

Human IgM solution (Sigma-Aldrich) was buffer-exchanged with 200 mM aqueous ammonium acetate to achieve a final antibody concentration of  $\sim 1$  mg ml<sup>-1</sup>. A nano-ESI interface with a 20  $\mu$ m pico-emitter ESI needle (New Objective) was used

for IgM measurements. Colloidal gold nanoparticles with nominal diameters of 5 nm (mean diameter, 5.1 nm; variance, 19%) and 10 nm (mean diameter, 10.7 nm; variance, 10%) were purchased from Sigma-Aldrich. For ESI measurements, the gold nanoparticle sample was diluted using equal amounts of methanol and introduced into the ESI needle. The NEMS device was kept in the highest-vacuum chamber of a three-stage differential pumping set-up, with a base pressure of  $1 \times 10^{-5}$  torr before cryopumping took place. The typical operating temperature for the ESI sample stage was 70 K for the gold nanoparticle samples and 140 K for the IgM samples. The NEMS devices for both ESI and MALDI set-ups were cooled to prevent captured particles from rapidly desorbing from the device surface.

The MALDI sample plates were prepared by washing the stock colloid solutions in water. Using a centrifuge, the solutions were then concentrated to  $\sim 5 \times 10^{14}$  particles per ml and  $1 \times 10^{14}$  particles per ml for the 5 and 10 nm gold nanoparticle samples, respectively. For each sample, 38  $\mu$ l of solution was drip-dried onto 3-mm-diameter spots on a pyrex sample plate. The glycerol samples were prepared by adding glycerol (Sigma-Aldrich; concentration, 10%) to the gold nanoparticle solution before drying on the pyrex sample plate. After drying in air, the plate was placed inside the vacuum chamber  $\sim 0.5$  cm from the NEMS device. A nitrogen laser (model NL 100, Stanford Research Systems) was focused through a lens to a spot ( $\sim 50 \times 100 \mu\text{m}^2$ ) to illuminate the back side of the pyrex plate. The laser was operated at a wavelength of 337 nm, with 170  $\mu$ J per pulse, a pulse width of 3.5 ns and a repetition rate of 1 Hz. The chamber was maintained at a base pressure of  $1 \times 10^{-9}$  torr and the NEMS device stage was cooled to 80 K.

Received 24 February 2012; accepted 15 June 2012;  
published online 26 August 2012

## References

- Andersson, C.-O. Mass spectrometric studies on amino acid and peptide derivatives. *Acta Chem. Scand.* **12**, 1353 (1958).
- Beynon, J. H. The use of the mass spectrometer for the identification of organic compounds. *Microchim. Acta* **44**, 437–453 (1956).
- Domon, B. & Aebersold, R. Mass spectrometry and protein analysis. *Science* **312**, 212–217 (2006).
- Benesch, J. L. P. & Robinson, C. V. Mass spectrometry of macromolecular assemblies: preservation and dissociation. *Curr. Opin. Struct. Biol.* **16**, 245–251 (2006).
- Robinson, C. V., Benesch, J. L. P., Ruotolo, B. T. & Simmons, D. A. Protein complexes in the gas phase: technology for structural genomics and proteomics. *Chem. Rev.* **107**, 3544–3567 (2007).
- Warscheid, B., Oeljeklaus, S. & Meyer, H. E. New dimensions in the study of protein complexes using quantitative mass spectrometry. *FEBS Lett.* **583**, 1674–1683 (2009).
- Van Duijn, E., Barendregt, A., Synowsky, S., Versluis, C. & Heck, A. J. R. Chaperonin complexes monitored by ion mobility mass spectrometry. *J. Am. Chem. Soc.* **131**, 1452–1459 (2009).
- Heck, A. J. R. Native mass spectrometry: a bridge between interactomics and structural biology. *Nature Methods* **5**, 927–933 (2008).
- Ekinci, K. L., Huang, X. M. H. & Roukes, M. L. Ultrasensitive nanoelectromechanical mass detection. *Appl. Phys. Lett.* **84**, 4469–4471 (2004).
- Ilic, B. *et al.* Attogram detection using nanoelectromechanical oscillators. *J. Appl. Phys.* **95**, 3694–3703 (2004).
- Yang, Y. T., Callegari, C., Feng, X. L., Ekinci, K. L. & Roukes, M. L. Zeptogram-scale nanomechanical mass sensing. *Nano Lett.* **6**, 583–586 (2006).
- Li, M., Tang, H. X. & Roukes, M. L. Ultra-sensitive NEMS-based cantilevers for sensing, scanned probe and very high-frequency applications. *Nature Nanotech.* **2**, 114–120 (2007).
- Chiu, H.-Y., Hung, P., Postma, H. W. C. & Bockrath, M. Atomic-scale mass sensing using carbon nanotube resonators. *Nano Lett.* **8**, 4342–4346 (2008).
- Lassagne, B., Garcia-Sanchez, D., Aguasca, A. & Bachtold, A. Ultrasensitive mass sensing with a nanotube electromechanical resonator. *Nano Lett.* **8**, 3735–3738 (2008).
- Jensen, K., Kim, K. & Zettl, A. An atomic-resolution nanomechanical mass sensor. *Nature Nanotech.* **3**, 533–537 (2008).
- Naik, A. K., Hanay, M. S., Hiebert, W. K., Feng, X. L. & Roukes, M. L. Towards single-molecule nanomechanical mass spectrometry. *Nature Nanotech.* **4**, 445–450 (2009).
- Gil-Santos, E. *et al.* Nanomechanical mass sensing and stiffness spectrometry based on two-dimensional vibrations of resonant nanowires. *Nature Nanotech.* **5**, 641–645 (2010).
- Ekinci, K. L., Yang, Y. T. & Roukes, M. L. Ultimate limits to inertial mass sensing based upon nanoelectromechanical systems. *J. Appl. Phys.* **95**, 2682–2689 (2004).
- Siuzdak, G. *The Expanding Role of Mass Spectrometry in Biotechnology* (MCC Press, 2003).
- Hanay, M. S. *Towards Single-Molecule Nanomechanical Mass Spectrometry* PhD thesis, California Institute of Technology (2011).
- Roukes, M. L., Naik, A. K. & Hanay, M. S. Single molecule mass spectroscopy enabled by nanoelectromechanical systems. US patent 8,227,747 (2012).

22. Dohn, S., Sandberg, R., Svendsen, W. & Boisen, A. Enhanced functionality of cantilever based mass sensors using higher modes. *Appl. Phys. Lett.* **86**, 233501 (2005).
23. Dohn, S., Svendsen, W., Boisen, A. & Hansen, O. Mass and position determination of attached particles on cantilever based mass sensors. *Rev. Sci. Instrum.* **78**, 103303 (2007).
24. Schmid, S., Dohn, S. & Boisen, A. Real-time particle mass spectrometry based on resonant micro strings. *Sensors* **10**, 8092–8100 (2010).
25. Allan, D. W. Statistics of atomic frequency standards. *Proc. IEEE* **54**, 221–230 (1966).
26. Casella, G. & Berger, R. L. *Statistical Inference* 2nd edn (Duxbury Press, 2001).
27. Bargatin, I., Kozinsky, I. & Roukes, M. L. Efficient electrothermal actuation of multiple modes of high-frequency nanoelectromechanical resonators. *Appl. Phys. Lett.* **90**, 093116 (2007).
28. Mile, E. *et al.* In-plane nanoelectromechanical resonators based on silicon nanowire piezoresistive detection. *Nanotechnology* **21**, 165504 (2010).
29. Caltech/CEA-LETI Alliance for Nanosystems VLSI, 200 mm (second generation) Standard NEMS process: 'CAL2'; available at <http://www.nanovlsi.com>.
30. Kharrat, C., Colinet, E. & Voda, A. in *Sensors, 2008 IEE Conference* 1135–1138 (IEEE, 2008).
31. Chiang, C. L., Hsu, M. B. & Lai, L. B. Control of nucleation and growth of gold nanoparticles in AOT/Span80/isooctane mixed reverse micelles. *J. Solid State Chem.* **177**, 3891–3895 (2004).
32. Kim, B., Carignano, M. A., Tripp, S. L. & Wei, A. Cluster size analysis of two-dimensional order in colloidal gold nanoparticle arrays. *Langmuir* **20**, 9360–9365 (2004).
33. Westcott, S. L., Oldenburg, S. J., Lee, T. R. & Halas, N. J. Formation and adsorption of clusters of gold nanoparticles onto functionalized silica nanoparticle surfaces. *Langmuir* **14**, 5396–5401 (1998).
34. Tanaka, K. The origin of macromolecule ionization by laser irradiation (Nobel Lecture). *Angew. Chem. Int. Ed.* **42**, 3860–3870 (2003).
35. Hughey, C. T., Brewer, J. W., Colosia, A. D., Rosse, W. F. & Corley, R. B. Production of IgM hexamers by normal and autoimmune B cells: implications for the physiologic role of hexameric IgM. *J. Immunol.* **161**, 4091–4097 (1998).
36. Collins, C., Tsui, F. W. L. & Shulman, M. J. Differential activation of human and guinea pig complement by pentameric and hexameric IgM. *Eur. J. Immunol.* **32**, 1802–1810 (2002).
37. Azuma, Y. *et al.* Recombinant human hexamer-dominant IgM monoclonal antibody to ganglioside GM3 for treatment of melanoma. *Clin. Cancer Res.* **13**, 2745–2750 (2007).
38. Lindhagen-Persson, M., Brännström, K., Vestling, M., Steinitz, M. & Olofsson, A. Amyloid- $\beta$  oligomer specificity mediated by the IgM isotype—implications for a specific protective mechanism exerted by endogenous auto-antibodies. *PLoS ONE* **5**, 13928 (2010).
39. Davis, A. C. & Shulman, M. J. IgM—molecular requirements for its assembly and function. *Immunol. Today* **10**, 118–128 (1989).
40. Bacher, G. *et al.* Charge-reduced nano electrospray ionization combined with differential mobility analysis of peptides, proteins, glycoproteins, noncovalent protein complexes and viruses. *J. Mass Spectrom.* **36**, 1038–1052 (2001).
41. Loo, J. A. *et al.* Electrospray ionization mass spectrometry and ion mobility analysis of the 20S proteasome complex. *J. Am. Soc. Mass Spectrom.* **16**, 998–1008 (2005).

### Acknowledgements

The authors thank I. Bargatin, E. Myers, M. Shahgholi, I. Kozinsky, M. Matheny, J. Sader, P. Hung, E. Sage and R. Karabalin for helpful discussions, and C. Marcoux for assistance with device fabrication. The authors acknowledge the support and infrastructure provided by the Kavli Nanoscience Institute at Caltech, as well as support from the NIH (grant no. R01-GM085666-01A1Z), the NSF (MRI grant no. DBI-0821863), the Fondation pour la Recherche et l'Enseignement Supérieur, an Institut Mérieux Research Grant, partial support from the Institut Carnot CEA-LETI and the Carnot-NEMS project, and a grant from the Partnership University Fund of the French Embassy to the USA. M.L.R. acknowledges support from an NIH Director's Pioneer Award and a Chaire d'Excellence (RTRA) from Fondation Nanosciences. S.H. and E.C. acknowledge partial support from EU CEA Eurotalent Fellowships.

### Author contributions

M.L.R., A.K.N., M.S.H. and S.K. conceived and designed the experiments. M.S.H., S.K. and A.K.N. performed the experiments. M.S.H., S.K., A.K.N. and M.L.R. analysed the data. M.S.H., S.K., A.K.N., D.C., S.H., E.C.B., E.C., L.D. and M.L.R. contributed materials and analysis tools. M.S.H., S.K., M.L.R. and A.K.N. wrote the paper.

### Additional information

Supplementary information is available in the online version of the paper. Reprints and permission information is available online at <http://www.nature.com/reprints>. Correspondence and requests for materials should be addressed to M.L.R.

### Competing financial interests

The authors declare no competing financial interests.